



# Role of quenching method on cooling rate and microstructure of steels: Variations in coolant and its flow arrangement

Sang Gun Lee<sup>a</sup>, Massoud Kaviany<sup>b</sup>, Jungho Lee<sup>a,\*</sup>

<sup>a</sup> Department of Mechanical Engineering, Ajou University, Suwon, Gyeonggi-do 16499, Republic of Korea

<sup>b</sup> Department of Mechanical Engineering, University of Michigan, Ann Arbor, MI 48109, USA

## ARTICLE INFO

### Article history:

Received 21 December 2021

Revised 6 February 2022

Accepted 9 February 2022

### Keywords:

Various quenching methods

Multiple jet quenching

Inverse heat conduction problem

Theoretical approximation

Microscopic examination

## ABSTRACT

During quenching of steel, the rate of heat removal from the surface and the local cooling rate of steel determine its microstructure. Here these rates are controlled by the extent of the force flow (e.g., single and multiple jets, forced and unforced immersion), coolant (e.g., water and oil), and steel (e.g., stainless or alloy). The steel plate is initially at 900°C is cooled with room-temperature coolants. The recorded temperature distribution within the object is used to compute the surface temperature and heat flux by solving the inverse heat conduction problem (IHCP). The high Biot number analytic solution of 1-D transient conduction in semi-infinite slab with prescribed surface temperature is also used as a reference for the ideal cooling condition. It is shown that the multiple water jet cooling results in the highest heat transfer rate (largest Biot number) and cooling rate, thus the desired martensite phase of the microstructure. On the other hand, the water forced immersion, water immersion, and oil immersion have a progressively lower cooling rate (smaller Biot number), and therefore, a smaller fraction of the martensite phase. Comparison of the IHCP and analytic results for the multiple water jets show that the IHCP underpredicts the cooling rate for the first 0.5 s.

© 2022 Elsevier Ltd. All rights reserved.

## 1. Introduction

The quenching process is a common thermal treatment aimed at an improved final product in steel manufacturing by inducing the required mechanical properties such as low residual stresses and high hardness. It involves heating the workpiece to a very high temperature and cooling it quickly (which involves boiling). The typical manufacturing process involves heating-holding, hardening (including a quench), and tempering stages. The heating-holding stage aims to transform the starting microstructure into a homogeneous austenitic phase (i.e., parent phase). The intensely heated steel is cooled down using various quenching techniques in the quench hardening stage. These include immersing in a coolant bath such as water or oil, coolant spraying using a nozzle, and submerged/free-surface jet impinging over the surface [1–8]. In this process, the parent austenitic phase is transformed into diverse microstructures such as ferrite, pearlite, bainite, martensite, and residual austenite. The desired microstructure phase distributions post quenching is obtained with different coolants and their flow arrangements [9–11].

Fig. 1 shows that the cooling rate strongly affects the surface morphology, structure, and composition of the quenched steel. This

CCT (continuous cooling transformation) diagram of the low-alloy steel (SNCM439) shows that the cooling curves affect the specific microstructure and deformation. The slow and moderate cooling mainly forms ferrite-bainite and bainite structures. Rapid cooling leads to a martensitic transformation because it can retain the high carbon contained in the parent austenitic phase. Martensite shows high strength and hardness because the dissolved carbon atoms strengthen the structure by interfering with the atomic planar slip. Therefore, rapid cooling is important for its desired strength and hardness to achieve martensitic transformation. In addition, it is essential to maintain the mechanical properties with the crystalline structure and the phase distribution that would be lost during slow cooling. As the carbon acts as a hardening agent, the strength of steel generally increases with the proportion of carbon it contains. This made the metal harder to weld and less ductile but harder and stronger. Low-carbon steel cannot be strengthened by heat treatment, which is only accomplished through cold working. This steel is machinable and weldable due to its softer and excellent ductility [12]. However, martensite, which contains high residual stress due to intensive cooling, can cause defects (i.e., distortion and cracking). So, it is necessary to carefully design the optimal quenching method to form microstructural uniformity without surface cracking.

Among various quench methods, immersion quenching is widely used to minimize the formation of undesirable thermal

\* Corresponding author.

E-mail address: [jungholee@ajou.ac.kr](mailto:jungholee@ajou.ac.kr) (J. Lee).

### Nomenclature

Bi	Biot number
$c_p$	heat capacity, J/kg-K
$C$	$\rho c_p$ , volumetric heat capacity, J/m <sup>3</sup> -K
$h$	heat transfer coefficient, W/m <sup>2</sup> -K
$L_c$	characteristic length, m
$k$	thermal conductivity, W/m-K
Nu	Nusselt number
$q$	heat flux, W/m <sup>2</sup>
$r$	radial location, m
$s$	unit step function
$t$	time, s
$T$	temperature, °C or K
$u$	jet exit velocity, m/s
$Y$	surface temperature variation
$z$	location from the surface, m
$\Sigma$	sum of squared function

### Greek

$\alpha$	thermal diffusivity, m <sup>2</sup> /s
$\lambda$	time step, s
$\Delta$	difference
$\rho$	density, kg/m <sup>3</sup>
$\zeta$	sensitivity coefficient

### Subscripts/superscripts

$c$	estimated value
$f$	fluid
$j$	temperature measured position
$k$	elapsed time
$L$	measured value
$m$	measured value
$s$	surface

and transformational gradients, which may lead to distortion and cracking [1,11]. The used coolants include water, oils, and aqueous polymer solutions. The current state-of-the-art quenching technology provides comparative data and its limitations. Bates [13] noted that direct immersion into highly subcooled water could cause large temperature differences within the workpiece. This can cause unpredictable distortion with detrimental post-quenching effects. Other coolants such as oil or polymers are used for a lower cooling rate, which improves temperature uniformity to minimize this distortion. However, the low cooling rate results in some precipitation that impairs the strength and the corrosion resistance of the steel.

Kobasko et al. [14,15] suggested the intensive quenching (IQ) method to harden the steel and patented the IntensiQuench<sup>SM</sup> process with a high water flow rate over the upper part of hot steel. They showed the cool rate several times faster than conventional quenching (e.g., immersion quenching). They showed a very high cooling rate required for a large martensite phase fraction. It was also found that rapid and uniform cooling could reduce the workpiece cracking and distortion while improving the hardness and durability of steel. The IQ technique is renamed as a forced quenching method and used here.

Another quenching technique widely used for rapid cooling is the impinging jet. The water jet from leaving the nozzle is directed to the workpiece surface with high inertia resulting in a high cooling rate [16]. Several investigations have focused on the boiling heat transfer characteristics of jet impingement quenching. Wolf et al. [5] have reviewed jet impingement hydrodynamics, identifying various boiling regimes and key factors. Their visual observation of boiling phenomena includes forming a dark zone beneath the circular region of the jet. Karwa et al. [8] reported that the surface temperature of this relatively dark zone was approximately 500 °C and is called the peripheral boundary or the wetting front. Ishigai et al. [17] reported that film boiling was not observed in the jet stagnation region, even with initial temperatures of over

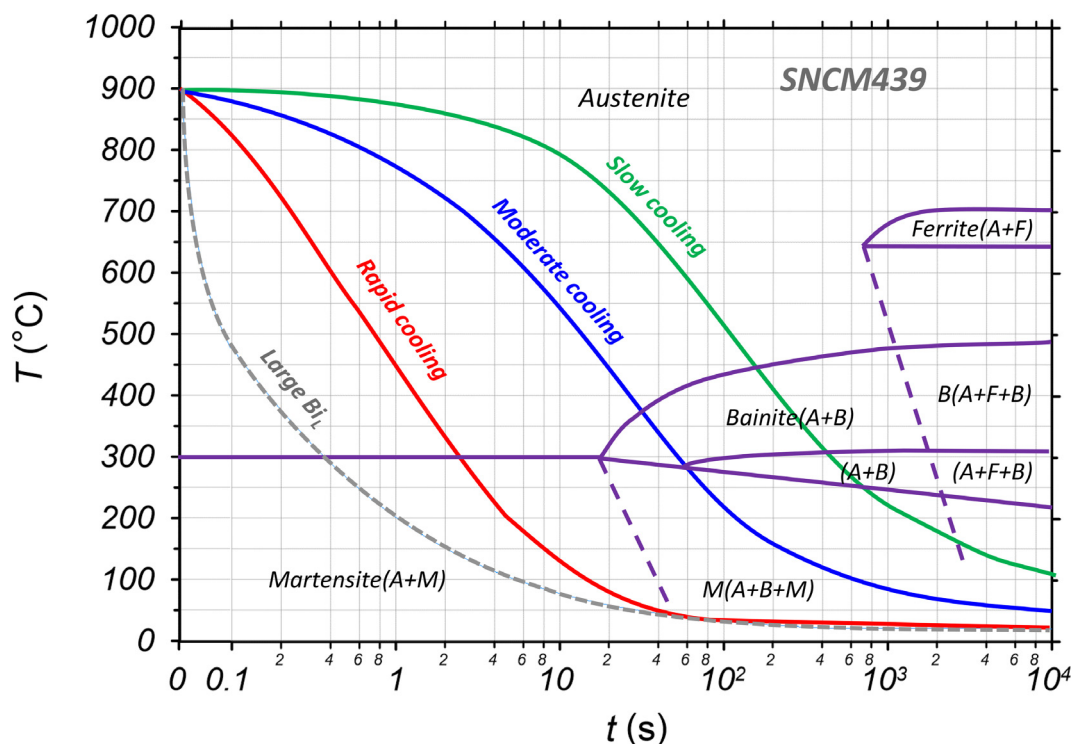


Fig. 1. CCT diagram of SNCM439 alloy steel under various cooling rates and the associated solid phase.

1000 °C. Hammad et al. [18] reported the existence of maximum heat flux in the nucleate boiling regime that changes into transition boiling within the fully-wetted region with its specific location varying with the surface wetting conditions. In our previous work with large superheated plates at 900 °C, the complex boiling phenomena for single and two interacting jets were identified [19,20]. The heat transfer coefficient enhancement due to the interaction of multiple jets was investigated, and the staggered arrangement and the optimal jet-to-jet spacing were also reported [21–24]. The multiple jets impinging with staggered array nozzles are also used in the present study.

In this study, we perform experiments with induction heating and four quenching methods, namely water and oil immersion, water forced immersion, and water multiple jet impingements, and compare their cooling performance by analyzing the post-quench microstructure and mechanical properties. We use water and oil coolants. We used embedded thermocouples within the workpiece and then used the 2-D inverse heat conduction problem (IHCP) to obtain the surface temperature and the corresponding surface heat flux. For the ideal, highest cooling rate (controlled by internal thermal resistance), we use the high Biot number, 1-D tran-

sient conduction analytic solution for comparison. We use two steel blocks, namely the stainless steel (SUS310S) and the alloy steel (SNM439). Finally, we use the LePera etching to examine the martensite-phase distribution of the quenched surface.

## 2. Experiments and analyses

### 2.1. Experimental system

Fig. 2(a) shows a schematic and experiment setup for the immersion quenching. The initially heated specimen is vertically inserted into the otherwise isothermal ( $20 \pm 0.5$  °C) coolant (water or oil) bath by a pneumatic device. The transparent windows ( $200 \times 200$  mm<sup>2</sup>) on the front and rear allow for visualization of the quench boiling phenomena recorded by a color, high-speed CCD camera (Phantom® M320) at 1000 frames per second. 4 stirrers are installed on each corner of the bath, with controlled rotation up to 3000 rpm using an rpm meter to reduce the cooling time. Fig. 2(b) shows the water, forced-flow immersion, and multiple-jet quenching. The flow loop mainly consists of the test section, flow loop, bath, induction heater, and data acquisition

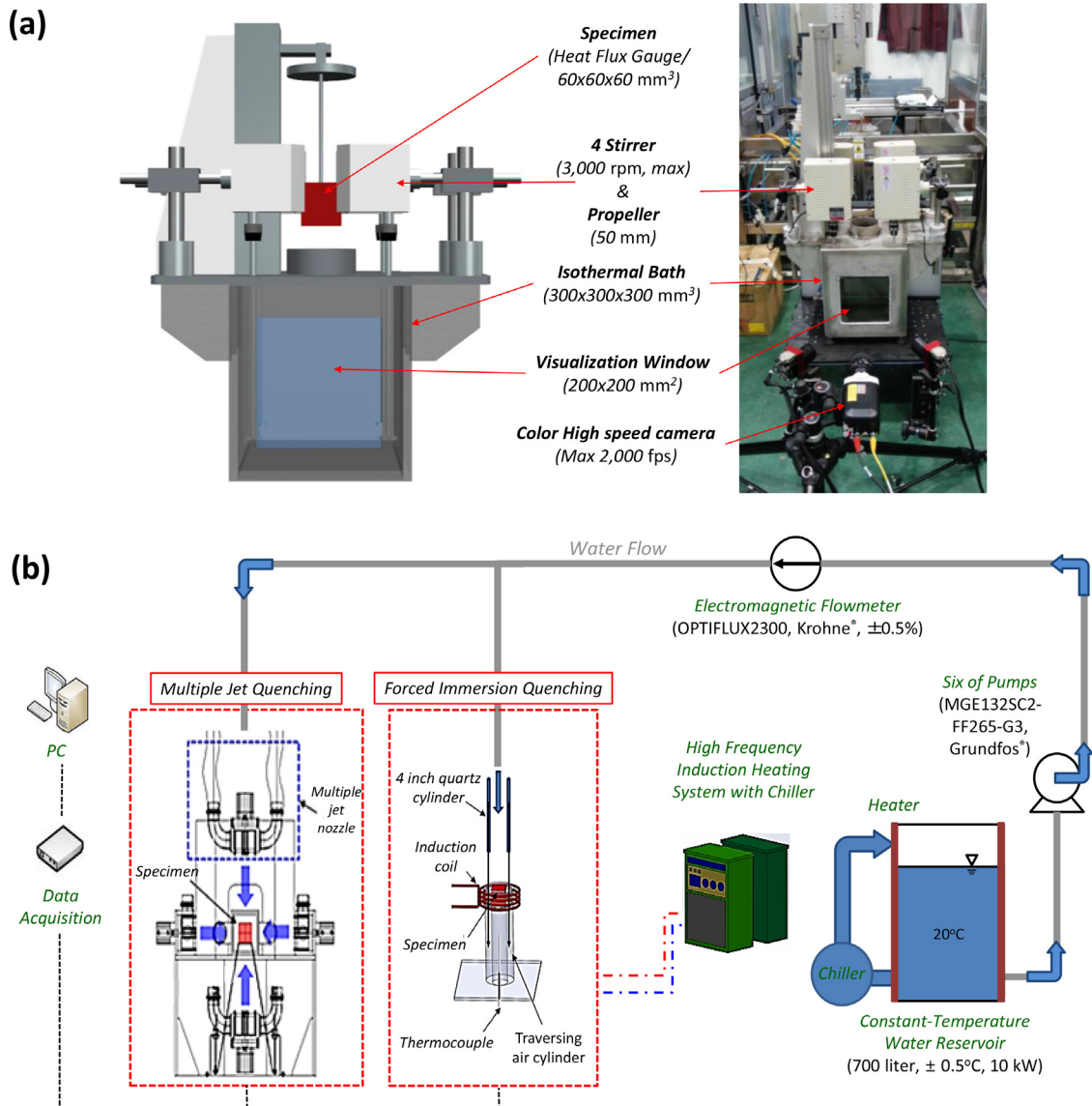
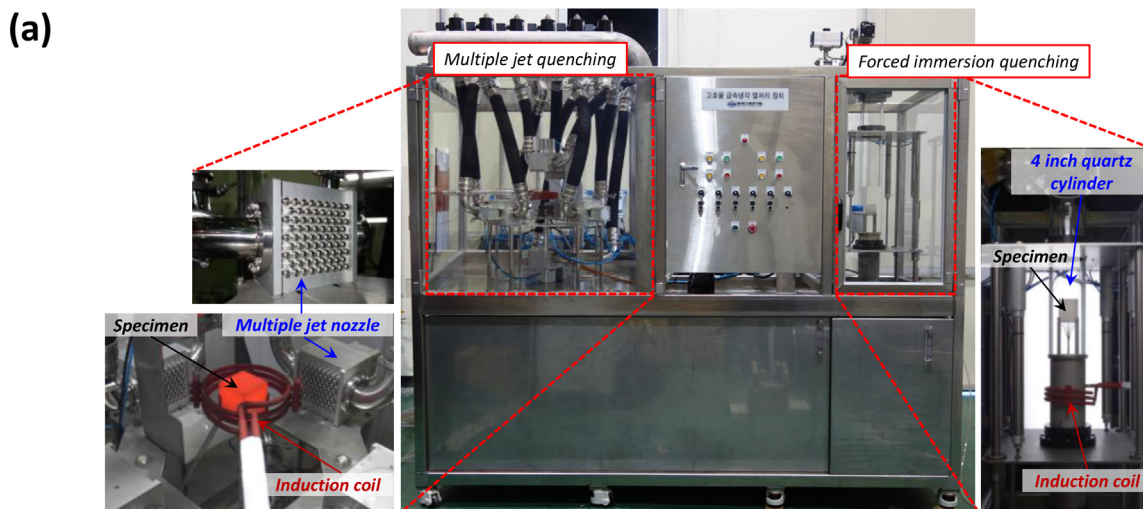
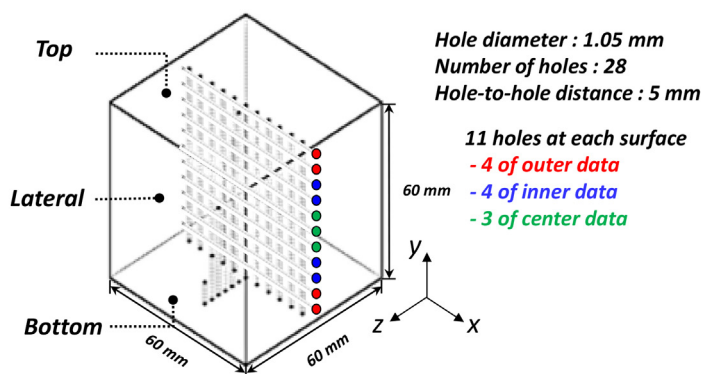


Fig. 2. Experimental system for (a) water/oil immersion quenching method and (b) forced immersion and multiple-jet quenching methods.



(b)

(i) Stainless steel (SUS310S)



(ii) Alloy steel (SNM439)

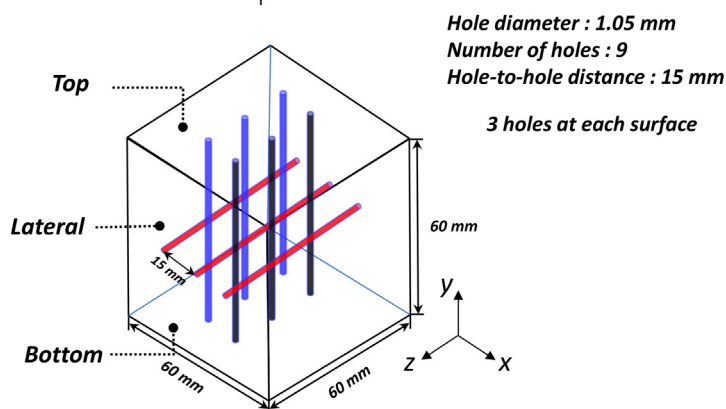


Fig. 3. (a) A photo of the system. (b) Image of steel cube and schematic of the thermocouple-holes for measuring temperature for (i) stainless steel (SUS310S) and (ii) alloy steel (SNM439).

Table 1  
 Uncertainty analysis for the estimated surface temperature and heat flux.

Uncertainty of Influence coefficient	Measured temperature variation( $\Delta T^m$ )	$\pm 5$	$^{\circ}\text{C}$
	Thermal conductivity ( $k$ )	10	%
	Heat capacity ( $c_p$ )	4.8	%
Uncertainty of Estimated heat flux	Heat flux range	0.5 ~ 5	$\text{MW/m}^2$
	Combined standard uncertainty	0.026 ~ 0.38	$\text{MW/m}^2$
	Total absolute uncertainty	0.052 ~ 0.76	$\text{MW/m}^2$
	Relative expanded uncertainty	10 ~ 15	%

system. The coolant temperature is maintained using a constant-temperature system made of an insulated stainless steel tank of 700 L, a 10 kW electric heater, six pumps (MGE132SC2-FF265-G3, Grundfos) capable of up to 25 m<sup>3</sup>/h each, and electromagnetic flowmeters (OPTIFLUX2300, Krohne). Fig. 3(a) is a photo of the experimental apparatus showing the forced immersion and multiple jet quenching designed as one system. During the forced immersion, water flows from the six pump lines into one large and enters the transparent (quartz) cylinder of diameter 102 mm. The total flow rate is adjusted as 60, 90, 120 m<sup>3</sup>/hr and falls under gravity over the upper part of the sample. In multiple-jet quenching, six nozzles surround the six faces of the cubic specimen (top, four lateral, and bottom faces). The nozzles are made of stainless steel tubes, and more details are given in Kim et al. [21] and Lee et al. [22].

The test assembly consists of the test block, an induction heating system, porous ceramic insulation, and thermocouples. A photo

of the cubic test block and the embedded thermocouples used as heat-flux gauges are shown in Fig. 3(b). The cubic has a side length of 60 mm, and two steel types are used in the comparison. Fig. 3(b)(i) shows the stainless steel (ANSI 310S) cube, which avoids phase-transformation heat generation that occurs in most carbon steels and is well known for its chemical inertness at elevated temperatures. This steel also does not undergo solid-solid phase transformation, releasing large latent heat causing temperature changes during the quenching process. Twenty-eight 1.0 ± 0.1 mm diameter holes were drilled with electric discharge machining (EDM). Twenty-two holes 59 mm deep and radially 5 mm apart are placed near the surface. Six holes with depths of 5, 15, 30, 45, 52, and 58 mm are placed near the center. Fig. 3(b)(ii) shows the SNCM439 low-alloy steel and compares post quench microstructure and mechanical surface properties. Nine holes, 59 mm deep, and three holes arranged with an interval of 15 mm on each surface (top, lateral and bottom). The K-type thermocouples (KMTXL-040G-6,

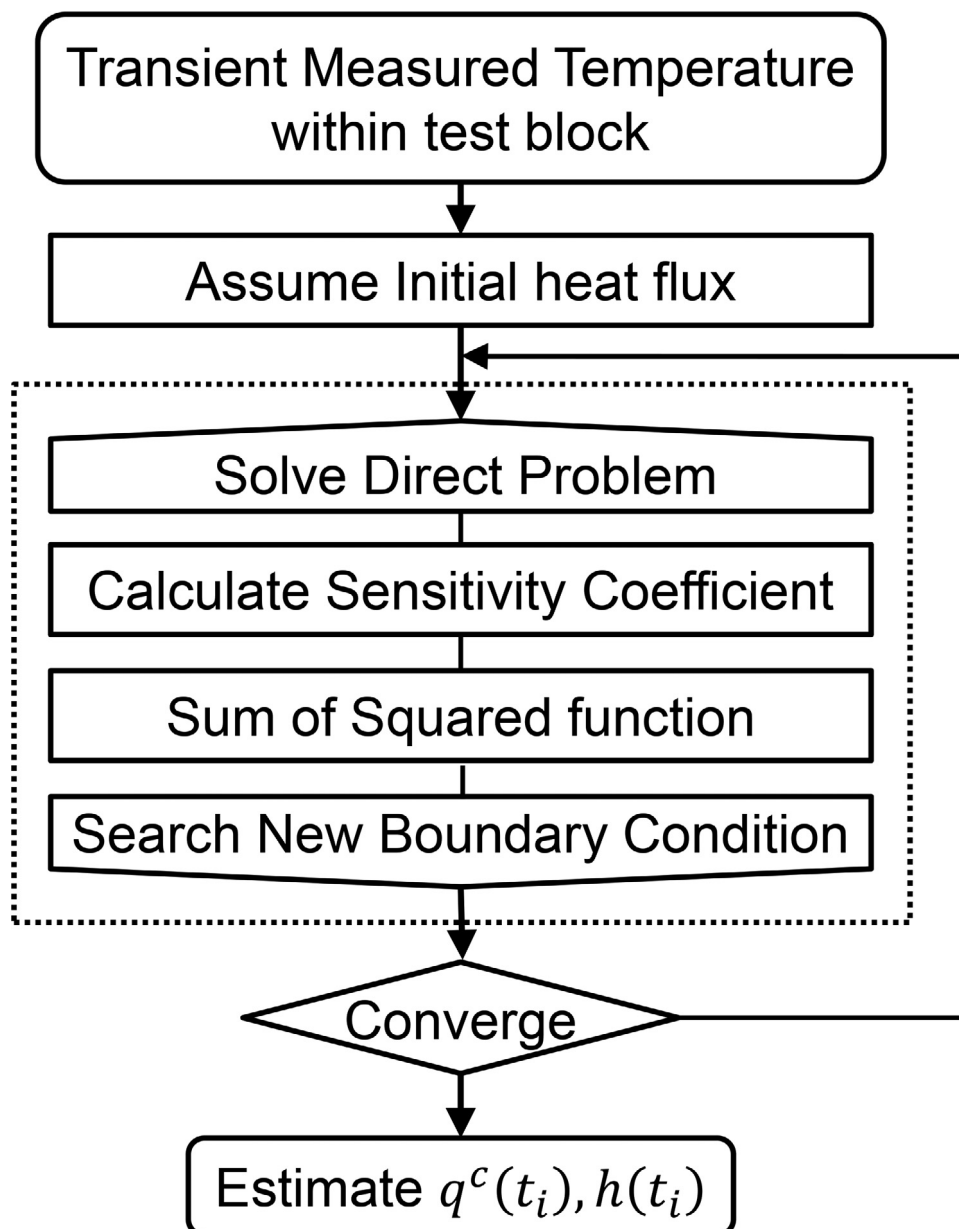


Fig. 4. Flowchart of the 2-D inverse heat conduction problem (IHCP) method for determining the transient surface temperature and heat flux based on the internal, measured temperature.

OMEGA®), 1 mm thick, are placed in these holes and spot welded. Thermocouple calibration is performed with a platinum resistance thermometer, and the uncertainty is found to be within 0.1 °C. Temperature is recorded with a high-speed data acquisition system (EX1032A, VTI Instruments Co.) at 10 data/s.

Induction heating is used to heat the specimen to over 900 °C, which is the austenite transition temperature. This noncontact heating uses a rectangular-shaped coil designed for uniform heating. A cylinder-shaped coil unit with a diameter of 13 mm is placed around the block. An AC with a frequency of 19 kHz is applied to the coil, and eddy currents are generated on the surface of the plate (Faraday law). So, the Joule heating is the product of the electrical resistance of the material and square of the induced current. The eddy current is uniformly distributed within the block, raising its temperature (within 20 min) to 1000 °C within 5 °C across the block.

2.2. Inverse heat conduction problem analysis

Since surface temperature measurement with surface-contact thermocouple interferes with the surface-convection cooling and installing surface heat flux meters on the surface causes similar interference, both the surface temperature and heat flux are deduced from the internal thermocouple readings. This is done using the so-called numerical inverse method, i.e., the inverse heat conduction problem (IHCP) with the formulation given by Twomey [25] and Beck et al. [26]. Fig. 4 shows the flowchart of this two-dimensional IHCP analysis. The measured data is imported into the computational nodes of the 2-D IHCP domain with nodal positions overlapping with some of the thermocouple locations. Based on experimental data, the initial temperature of the positions other than the thermocouple locations is calculated by interpolation. The initial surface heat flux is also estimated. And the temperature distribution is updated by the direct problem where the estimated boundary condition is used in the temperature distribution. Since

the IHCP is sensitive to measurement errors, the sensitivity coefficient ( $\zeta$ ) is adopted to improve the experimental design. The sensitivity coefficient is defined as the first derivative of a dependent variable, such as temperature, concerning the estimated heat flux. This sensitivity coefficient is expressed as [27]

$$\begin{aligned} \partial T_{i,j}(y, r, t) &= \partial T_{i,j}^*(y, r, t) + \left. \frac{\partial T_{i,j}^*(y, r, t)}{\partial q_i} \right|_{q_i=q_i^*} (q_i - q_i^*) \\ &\approx \partial T_{i,j}^*(y, r, t) + \zeta_{i,j}(q_i - q_i^*) \end{aligned} \tag{1}$$

where the superscript \* indicates the former time iteration. The calculated data is applied to the sum of squared functions (SSF) to search for an optimized boundary condition, minimizing the SSF, which is set as the difference between the measured temperature and the calculated temperature,

$$SSF = \sum_{j=1}^N (T_{i,j}^m(y, r, t) - T_{i,j}^c(y, r, t))^2 \tag{2}$$

where  $N$  is the total number of measured points.

The local, instantaneous (at elapsed time  $t_i$ ) heat transfer coefficient  $h(t_i)$  uses the surface temperature  $T(0, r, t_i)$ , surface heat flux ( $q$ ), and the coolant temperature  $T_\infty$  (20 °C)

$$h(t_i) = \frac{q^c(t_i)}{0.5[T^c(0, r, t_i) + T^c(0, r, t_{i-1})] - T_\infty} \tag{3}$$

where  $T^c(0, r, t_i)$  and  $q^c(t_i)$  are the estimated temperature and heat flux at the time ( $t_i$ ), and  $h$  is generally more accurate when evaluated at  $t_{i-1/2}$ .

The estimated surface heat flux is determined from the Fourier law by differentiating the calculated temperature using the Duhamel theorem [25] as

$$q^c(t_i) = -k \left. \frac{\partial T^c}{\partial z} \right|_{z=0} = -k \int_{t_0}^t \frac{\partial s(z, t - \lambda)}{\partial z} \Big|_{z=0} Y'(\lambda) d\lambda \tag{4}$$

where  $Y(t_i)$  is the time-varying surface temperature and  $\lambda$  and  $s(z, t_i)$  is the time step and unit step function, respectively.

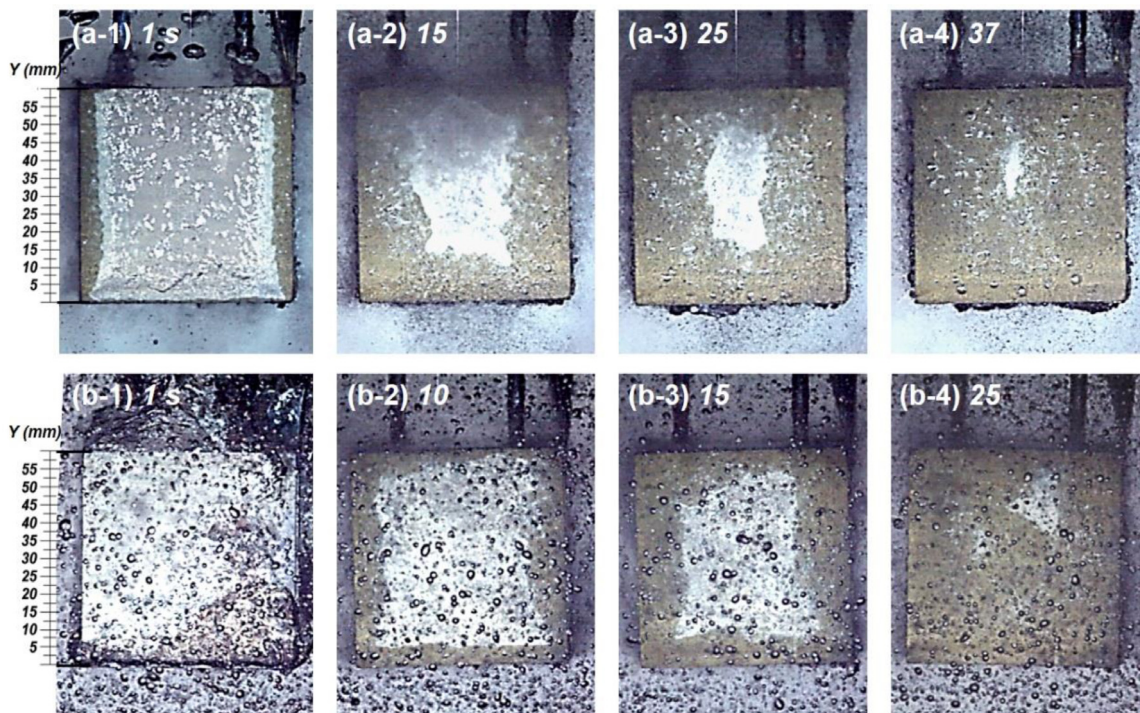


Fig. 5. A sequence of high-speed snapshot (time given in seconds) images of water immersion quenching on the lateral surface of the stainless steel (SUS310S) with stirrer speeds of (a) 0 and (b) 300 rpm.

As the estimates from IHCP in the initial stages of the quenching are affected by the quality of the thermal contact (between the test block and the thermocouple joint), a high conductivity paste is used to improve thermal contact. This contact resistance is assumed to be negligible in the IHCP. However, Gomez et al. [27] and Tenzer et al. [28] show the effect of this thermal resistance on the predicted heat flux for a short elapsed time cannot be ignored. So, the surface temperature and heat flux estimates for elapsed times up to 0.5 s should be excluded.

The uncertainty in the estimated heat flux combines the individual uncertainties, and this relation from ISO [29] and Blackwell

and Beck [30] is

$$\begin{aligned} \delta q^c &= \sqrt{\sum_{i=1}^n \left( \frac{\partial q^c}{\partial x_i} \delta x_i \right)^2} \\ &= \sqrt{\left( \frac{\partial q^c}{\partial \Delta T^m} \delta \Delta T^m \right)^2 + \left( \frac{\partial q^c}{\partial k} \delta k \right)^2 + \left( \frac{\partial q^c}{\partial C} \delta C \right)^2} \end{aligned} \quad (5)$$

where  $\Delta T^m$ ,  $k$  and  $C$  are influence parameters for the estimated heat flux. The uncertainties are listed in Table 1 and show the uncertainties in the estimated surface heat flux is within 10 to 15%.

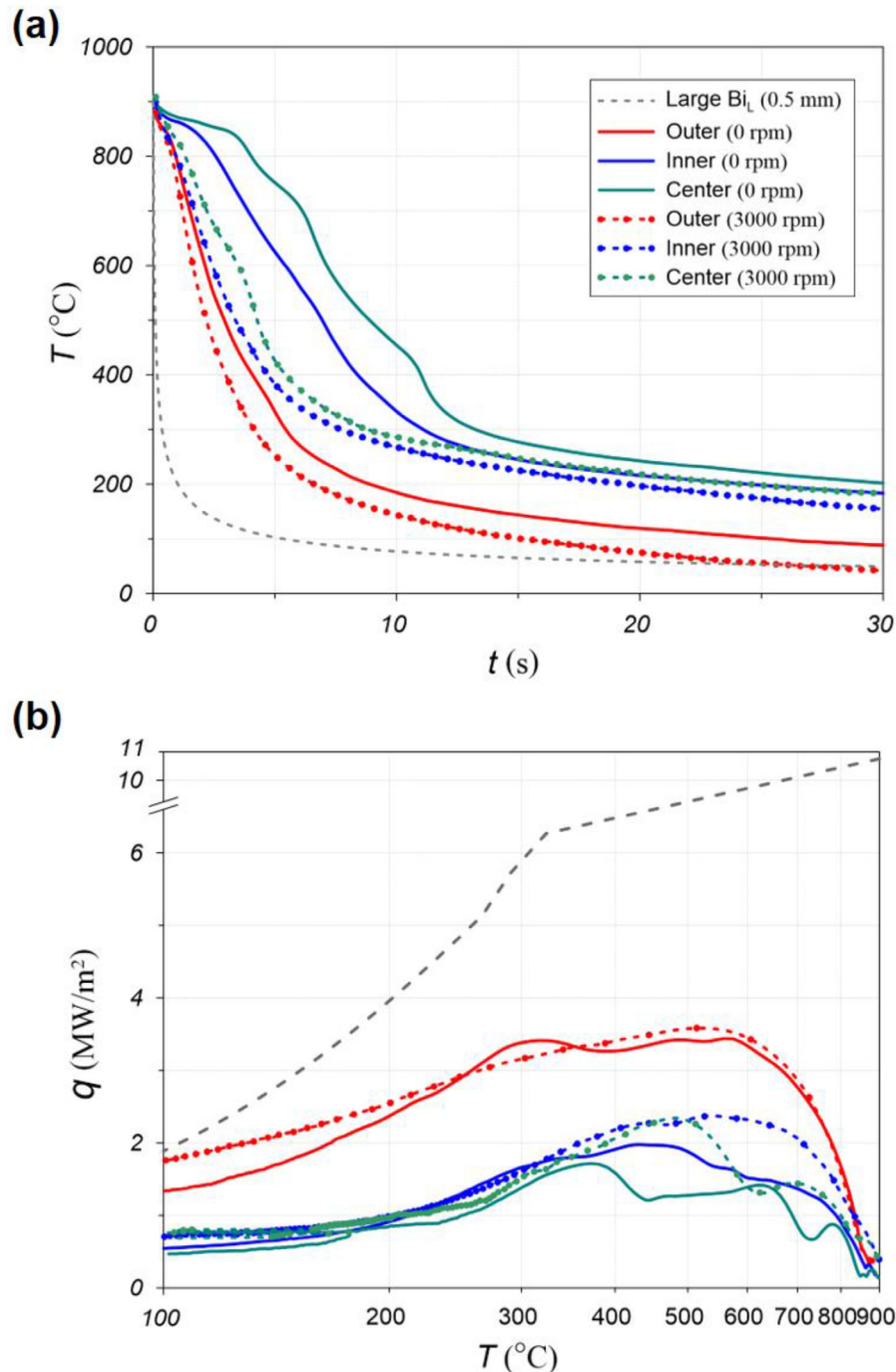
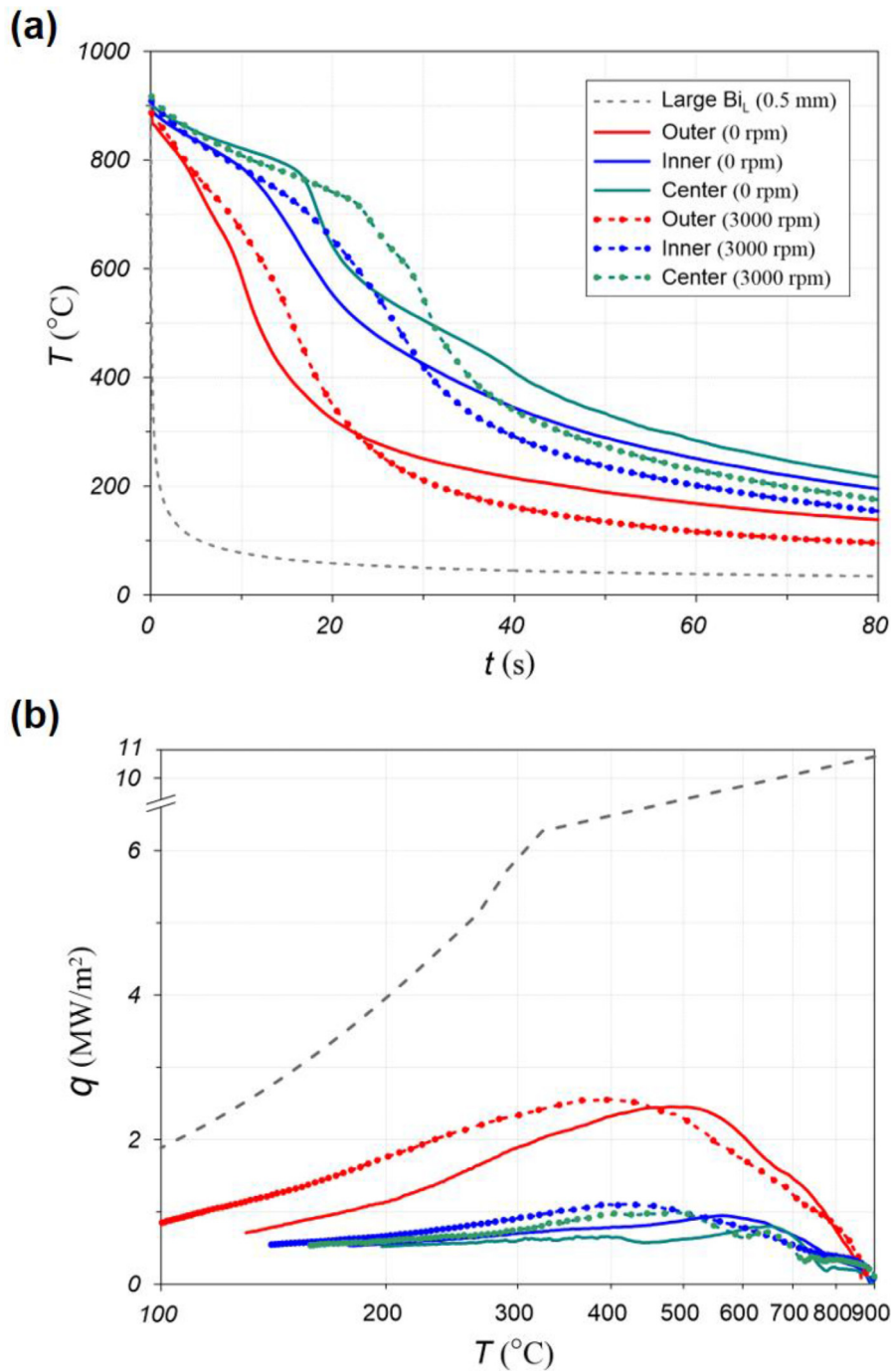


Fig. 6. (a) Temperature history and (b) surface heat flux-temperature for water immersion quenching of the stainless steel (SUS310S) at stirrer speeds of 0 and 3000 rpm at the outer, inner, and center positions.



**Fig. 7.** (a) Temperature history and (b) surface heat flux-temperature for oil immersion quenching of the stainless steel (SUS310S) at stirrer speeds of 0 and 3000 rpm at the outer, inner, and center positions.

### 2.3. Large Biot number analytical 1-D transient conduction analysis

In the surface-convection of cooling of a solid, the convection thermal resistance  $R_{t,ku}$  is considered external, while the conduction resistance within the solid  $R_{t,k}$  is considered internal. The ratio of the internal to external resistance is called the Biot number,  $Bi_L = R_{t,k}/R_{t,ku}$ . Under  $R_{t,k} \gg R_{t,ku}$  the temperature variation within the solid is much larger than the temperature difference between the surface and the incoming fluid. This is the so-called high Biot

number limit,

$$Bi_L = \frac{R_{t,k}}{R_{t,ku}} = \frac{(L/k_s A)}{(L_c/Nu_{L,c} k_f A)} = \frac{(L/k_s A)}{(1/hA)} = \frac{hL}{k_s} > 10, \quad \text{high-Biot number condition} \quad (6)$$

where  $L$  represents the conduction path within the solid (here we use the plate thickness) and  $L_c$  is the characteristic length used in

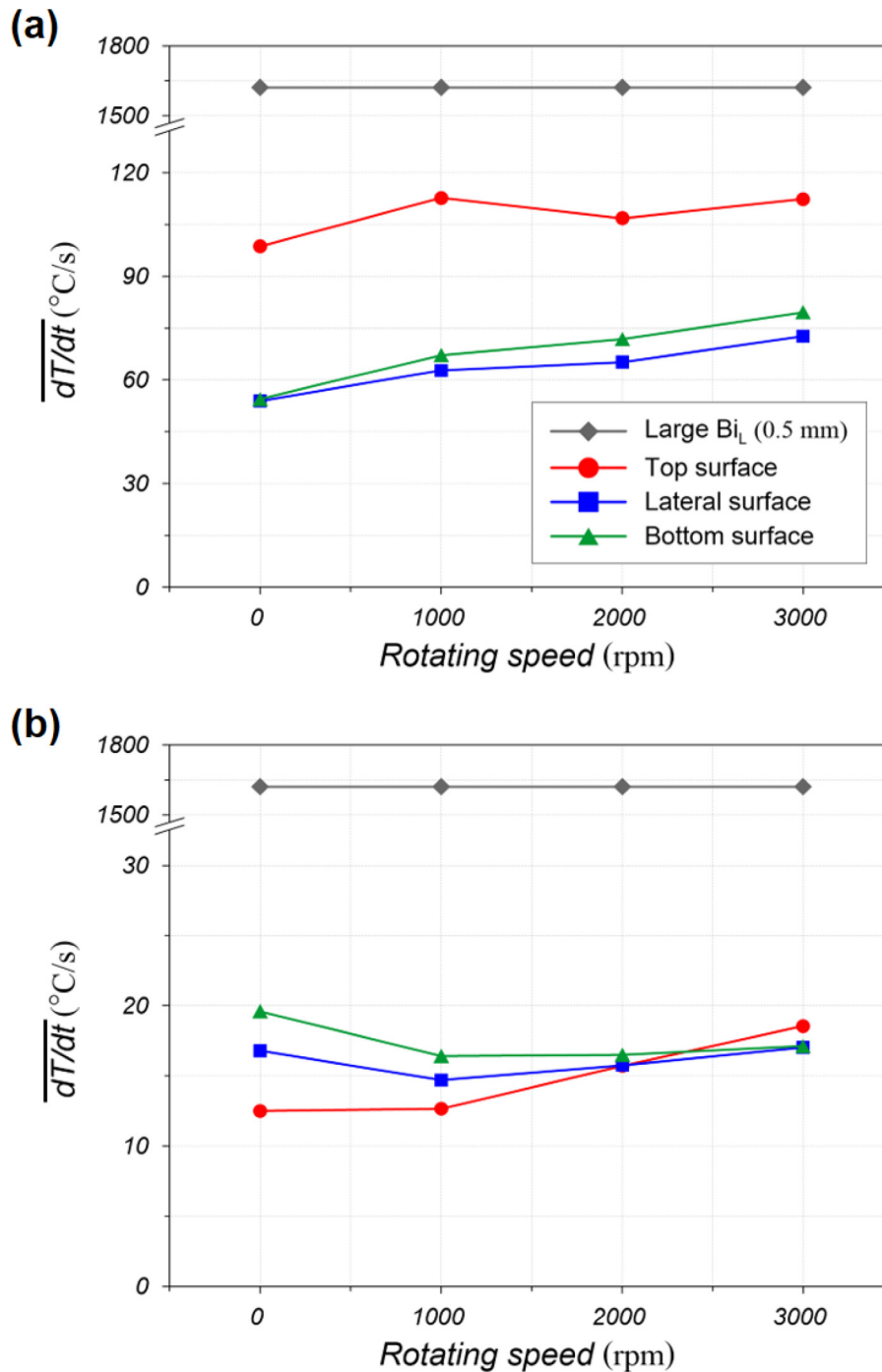


**Fig. 8.** Comparison of average cooling rate (over surface temperature from 900 to 300 °C) of (a) water and (b) oil immersion quenching of the stainless steel (SUS310S) with the various stirrer speeds.

the surface convection. The heat transfer coefficient is defined in terms of the Nusselt number  $h = Nu_{L,c} k_f / L_c$ .

Under  $Bi_L < 1$ , the uniform solid temperature (lumped-capacitance transient conduction) is assumed (does not apply to the quenching problem here). As will be shown, for quenching considered here, we have  $1 < Bi_L < 10$ . The closer it is to 10, the more justified is the constant surface temperature (equal to the coolant approaching temperature) assumption. For  $Bi_L$  approaches 1, both the internal and external thermal resistances are important. The analytical 1-D transient conduction solution is expressed in the form of series that also depends on the elapsed time.

For large  $Bi_L$ , the similarity solution assumes the slab is infinitely thick during the elapsed time of quenching (tens of seconds). This semi-infinite slab transient conduction solution ( $0 \leq t < \infty$ ,  $0 \leq x < \infty$ ), has a similarity variable and solution [31]

$$T(x, t) = T(t=0) + [T_s - T(t=0)] \left\{ 1 - \operatorname{erf} \left[ \frac{x}{2(\alpha t)^{1/2}} \right] \right\},$$

$$\operatorname{erf}(z) = \frac{2}{\sqrt{\pi}} \int_0^z e^{-z^2} dz, \quad \text{large } Bi_L \quad (7)$$

where  $\alpha$  is the solid thermal diffusivity,  $T(t = 0)$  is the initial, uniform temperature and  $T_s$  is the constant surface temperature (same as the coolant temperature and high Biot number).

The surface heat flux decreases with time and is

$$q = \frac{(\rho c_p k)_s^{1/2} [T_s - T(t = 0)]}{(\pi t)^{1/2}}, \quad \text{large } Bi_L \quad (8)$$

where  $(\rho c_p k)_s^{1/2}$  is the solid thermal effusivity.

The time rate of change of the temperature is found from the time derivative of Eq. (7) and the result is

$$\frac{\partial T(x, t)}{\partial t} = \frac{[T_s - T(t = 0)]}{2\pi^{1/2}\alpha^{1/2}t^{3/2}} x e^{-\frac{x^2}{4\alpha t}}, \quad \text{large } Bi_L \quad (9)$$

These results show the surface heat flux decreases with  $t^{-1/2}$ , and the time rate of temperature change drops much faster as  $t^{-3/2}$ .

The above results are valid until the temperature change reaches the opposite side of the plate,  $x = L$ , and this elapsed time  $t_o$  is

$$t_o = \frac{L^2}{3.6^2\alpha}, \quad \text{penetration time} \quad (10)$$

#### 2.4. Surface microstructure analysis and mechanical properties

The post quenching surface microstructure is observed by scanning electron microscopy (SEM) and the surface mechanical properties are measured. The surface is etched by the LePera (4% Picric acid, 1% Sodium metabisulfite) technique for 30 s, and the etched surface appears in different colors depending on the solid phase. For example, the ferrite phase appears brown, the martensite and unchanged austenite phases appear white, and the bainite phase is black [32–34]. After phase identification, the volume fraction of the bainite (plate-like microstructure) is optically measured using the Leopard image analyzer based on ASTM E112(E1382) guideline. Here, the martensitic and bainite phases are light blue and red regions for enhanced contrast. Although the light gray area includes the unchanged austenite, its fraction in the quenched steel is negligible in most cases. After phase quantification, the hardness and the sample elongation are measured, using the hardness profile after removing the decarburized layer of about 200  $\mu\text{m}$  from the

surface. The hardness is examined up to 10 mm from the surface at an interval of 0.05 mm. The elongation test is used to evaluate the cooling uniformity.

### 3. Results and discussion

#### 3.1. Comparison of heat transfer analysis

Fig. 5 is a snapshot from the high-speed video imaging of the water immersion quenching at the lateral surface of the sample. The effect of rotation is also shown. The complex boiling phenomena can be observed, e.g., film, nucleate boiling, and single-phase convection. For a short elapsed time, in Fig. 5(a-1) and (b-1), vapor film (light gray) is observed overall surface where the high-temperature surface remains unwetted. The light brown region represents a wetted surface and expands with time. The white bubbles on the surface are the nucleation sites where vigorous boiling occurs. Comparing Fig. 5(a) and (b), the brown region expands from the outside inward till collapse, and this collapsed time is shortened by 30% with the dynamic flow (rotation) around the surface.

Fig. 3(b)(i) shows locations of the measured temperatures, with three surfaces (top, lateral, and bottom), and the eleven measured data per surface are combined as the average value for the three different positions (outer, inner, and center). Fig. 5 shows the sequence of high-speed imaging during water immersion at the lateral surface. The effect of rotating speed is shown in no rotation of Fig. 5(a) and 3000 rpm of Fig. 5(b). Complex boiling phenomena such as film boiling, nucleate boiling and single-phase convection can be observed visually. At the initial elapsed time of Fig. 5(a-1) and (b-1), a vapor film (light gray) is observed on the entire surface, where the highly heated surface remains unwetted due to film boiling. Wetted surface (light brown) swell over time. White bubbles on the surface are nucleate sites where nucleate boiling occurs vigorously. Compared the Fig. 5(a) and (b), the wetted region generally expands from the outside to the inside of the surface, but the dynamic flow around the surface can reduce the fully wetted time by almost 30%.

The IHCP result for water and oil immersion is presented in Figs. 6 and 7. Oil has a high boiling point of 220  $^\circ\text{C}$  (1 atm) and low sensible heat, unlike water coolant. Therefore, the film

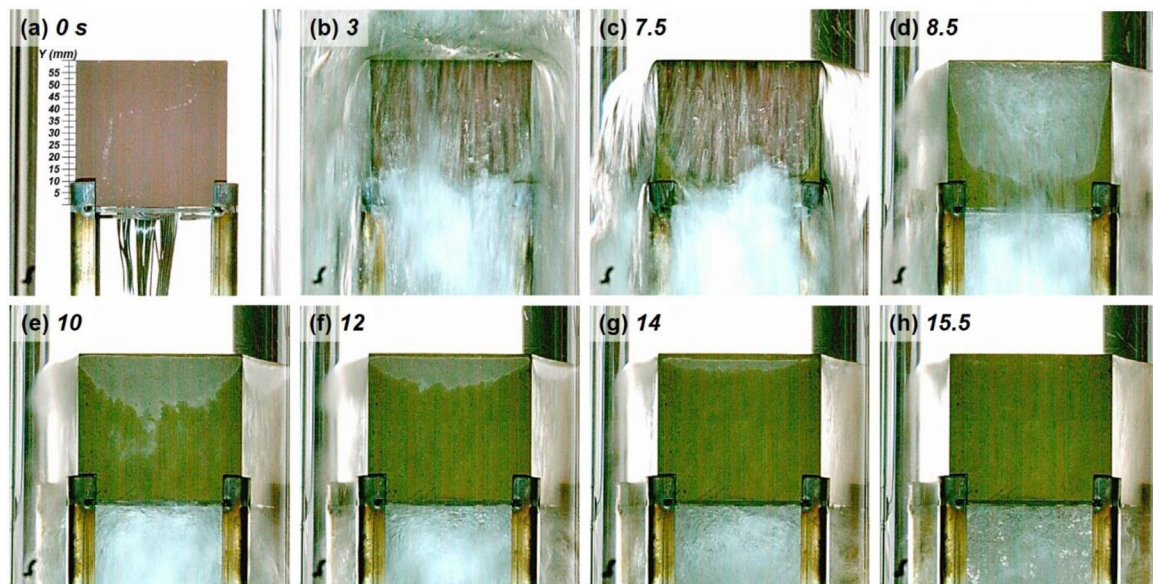


Fig. 9. Consecutive boiling visualization images of the forced immersion quenching of the stainless steel (SUS310S) on the lateral surface with a coolant flow rate of 60  $\text{m}^3/\text{hr}$ .

boiling regime can last longer. The nucleate boiling regime has lower heat transfer due to oil's low latent heat. Fig. 6 confirms that the position near the edge gets wet first, as shown in Fig. 5. Fig. 6(a) shows that the outer region cools first, followed by the inner and central regions. The surface heat flux history in Fig. 6(b) supports this, with the highest value of  $3.5 \text{ MW/m}^2$  found in the outer region. This slope becomes sharper with a rotating speed of 3000 rpm (dashed line). In addition, it is confirmed that the variations of the cooling rate at the three-position are reduced. The vapor film formed on the top and lateral surfaces is more readily shed than the bottom surface by buoyancy. The high surface flow

aids the cooling uniformity but does not eliminate it. In Fig. 7(a), each graph closely follows the local boiling regime occurring during an elapsed time period. There are three distinct stages: a gradual slope in the early stage, a large slope in the middle stage, and a modest slope in the final stage. These stages are associated with film boiling, nucleate boiling and single-phase convection. However, the outer region is preferentially cooled, similar to the water immersion. The boiling visualization is not performed on the opaque oil, but we expect that the film boiling disappears from the outer surface. The rotation does not improve the significant cooling rate and non-uniformity noticeably.

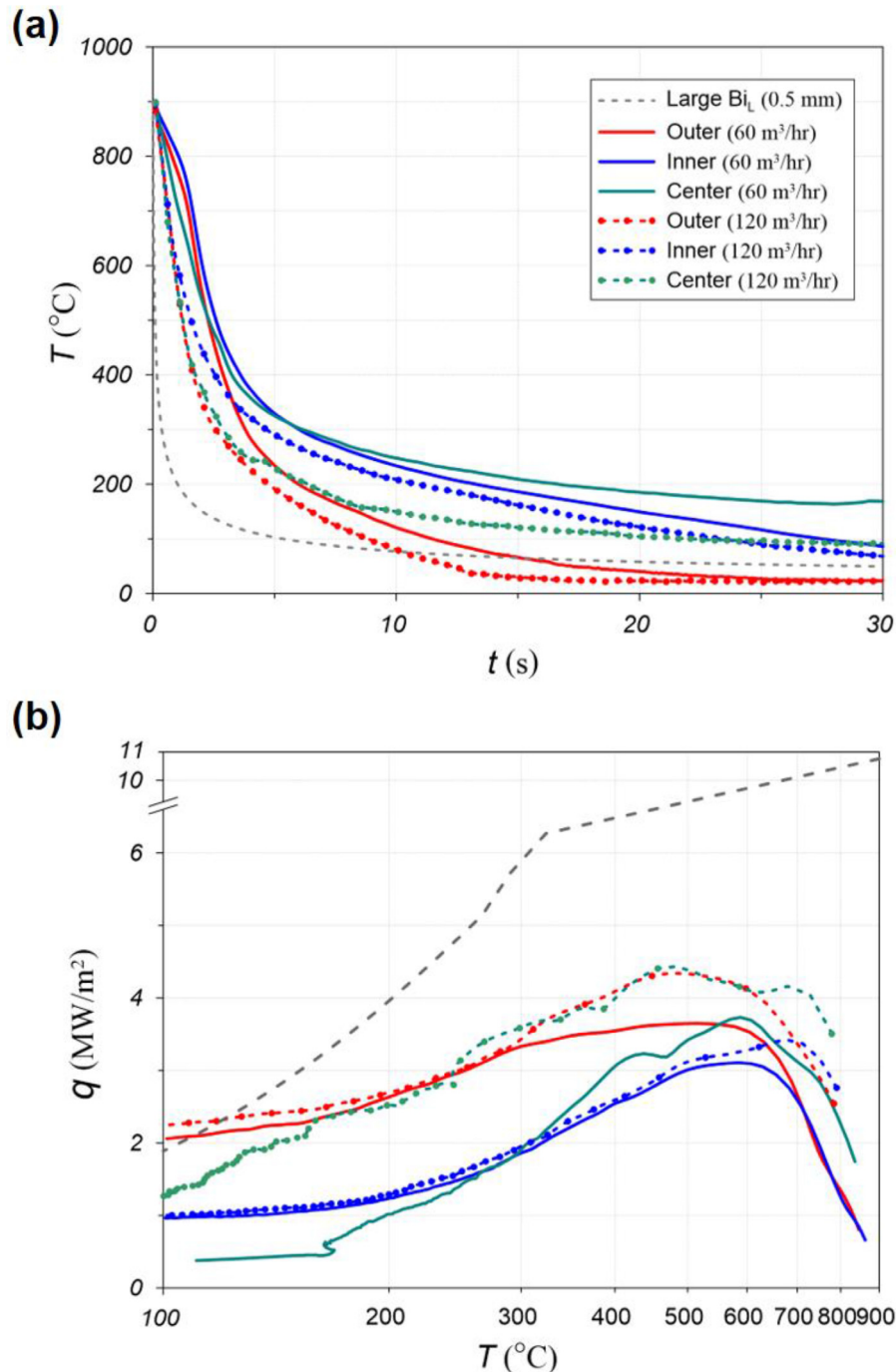


Fig. 10. (a) Temperature history, and (b) surface heat flux-temperature for forced immersion quenching of the stainless steel (SUS310S) with a coolant flow rate of 60 and 120 m<sup>3</sup>/hr at outer, inner, and center positions.

Fig. 8 compares the averaged cooling rate (over surface temperature from 900 to 300 °C) for the three surfaces (top, lateral, and bottom) of the water and oil immersion quenching and as a function of stirring speeds. The surface cooling capacity of water is almost 5 times higher than that of oil. The cooling rate for all surfaces (top, lateral, and bottom) becomes larger as the rpm increases for the water coolant. However, the cooling uniformity does not change. In contrast, the cooling uniformity of the oil coolant improves with the rotating speed and shows almost the same value at 2000 rpm.

Fig. 9 shows the snapshots from high-speed videography of the forced immersion quenching on the lateral surface. The transient boiling of forced immersion is divided into two; wetted and unwetted regions. Each region is accompanied by a boiling regime, the unwetted zone where film boiling with high resistance to heat transfer. The nucleate-boiling regime with a high heat transfer coefficient occurs in the wetted region, causing a sudden temperature drop which disappears in the transition-boiling regime. After that, the single-phase convection causes a gradual temperature drop. As shown in Fig. 9, the surface wetting starts from the bottom edge,

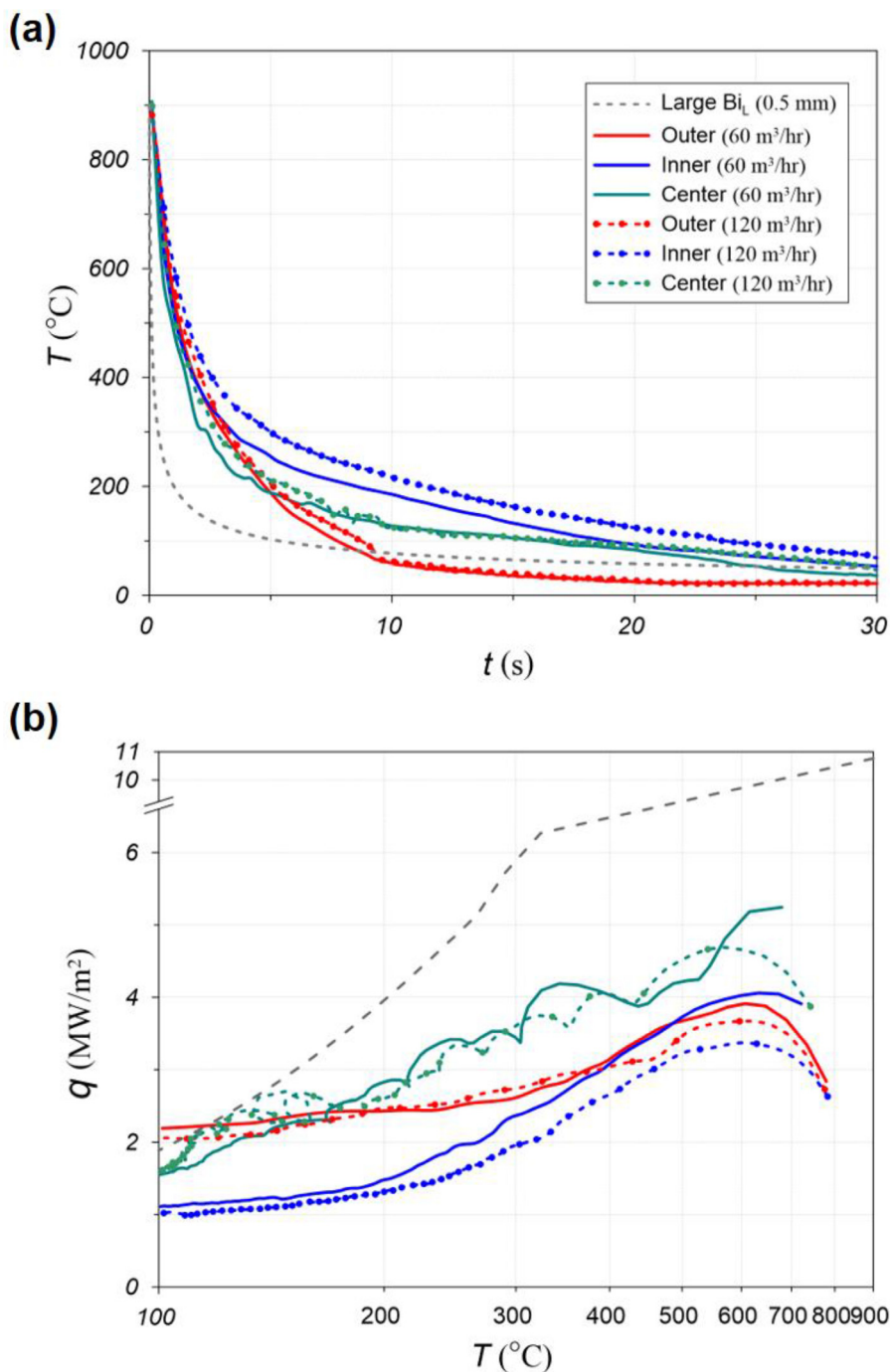


Fig. 11. (a) Temperature history, and (b) surface heat flux-surface temperature for the multiple-jet quenching of the stainless steel (SUS310S) with a coolant flow rate of 60 and 120 m<sup>3</sup>/hr, at outer, inner, and center positions.

which is attributed to flow separation from the top edge of the cube. The film boiling rapidly disappears from the bottom, and the nucleate boiling and single-phase convection cover the entire surface.

Figs. 10 and 11 show the transient temperature and surface heat flux distribution of forced immersion and multiple-jet quenching. There are for the flow rate of 60 and 120 m<sup>3</sup>/hr. For multiple-jet quenching (6 jets), the flow rate per surface is 10 and 20 m<sup>3</sup>/hr. Fig. 10(a) shows a sharper slope than the water/oil immersion of Figs. 6(a) and 7(a). Although film boiling exists due to flow separation,

as shown in Fig. 9, the high momentum of flow effectively improves the cooling. The difference in the cooling curve at different locations is greatly reduced. The enhancement in the heat flux is also confirmed in Fig. 10(b). The improvement is noticeable at a high coolant flow rate (dashed line) for 120 m<sup>3</sup>/hr; the cooling curves become steeper, and the surface heat flux increases. The multiple-jet impingement maximizes the flow dynamics, further improving the cooling performance. At 60 m<sup>3</sup>/hr, Fig. 11(a) shows a better cooling than Fig. 10(a). The cooling does not significantly change from 60 to 120 m<sup>3</sup>/hr. The film-boiling regime (grad-

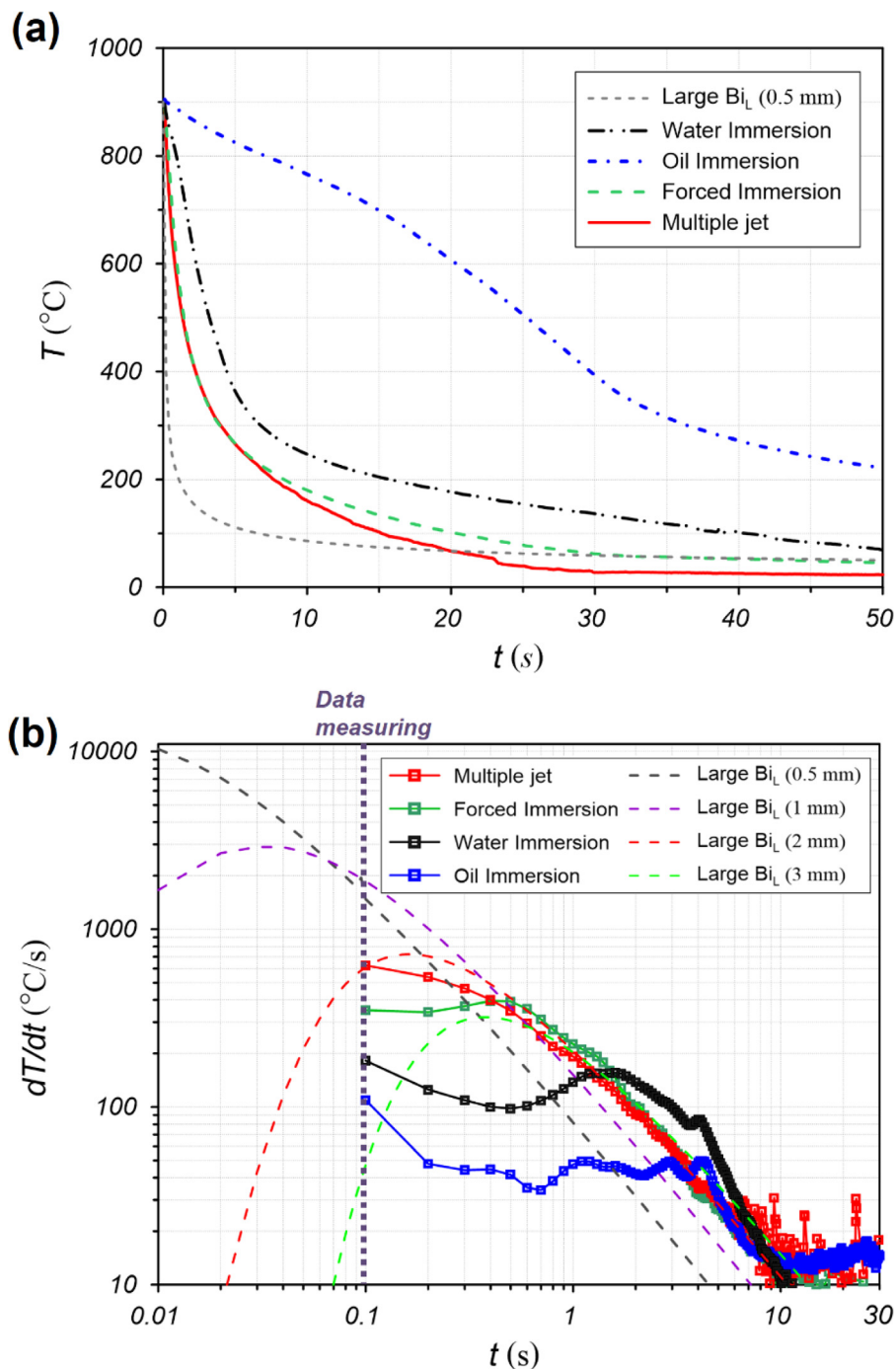


Fig. 12. Comparison of cooling performance of the stainless steel (SUS310S) for the four quenching methods of (a) temperature history and (b) local, time rate of change of temperature.

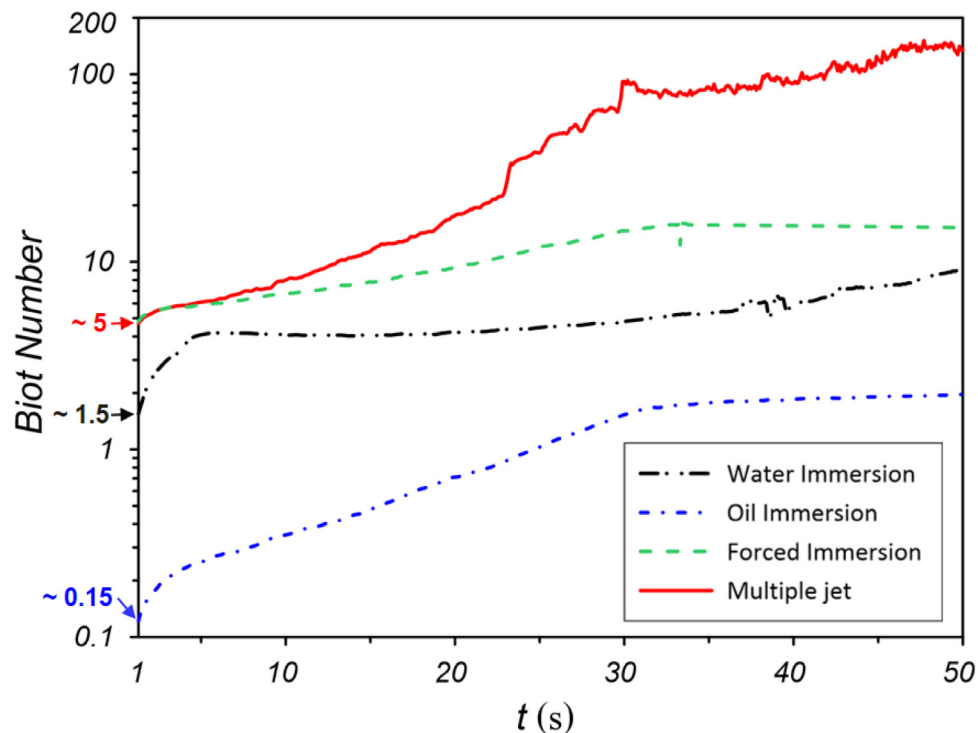


Fig. 13. Time variation of the Biot number for the four quenching methods (SUS310S stainless steel). There is an initial time delay in the IHCP method.

ual slope in the initial period) does not appear compared with the water/oil immersion. The high momentum flow efficiently removes the vapor film and induces nucleate boiling.

Finally, a comparison of the cooling performance of the four quenching methods is shown in Fig. 12. The most efficient conditions are used for the comparison, and Fig. 12(a) compares the averaged cooling history. The fastest is achieved with multiple-jet quenching. The next rapid cooling is by forced water and oil immersion. That means that the flow dynamics of jet impingement is the most effective method in rapid cooling. This is also confirmed with the cooling rate comparison in Fig. 12(b). The maximum cooling rate of multiple jet quenching is achieved at elapsed time of 0.1 s (although we do not expect high accuracy from the IHCP method for short elapsed time), which indicates the nucleate boiling regime occurs right after quenching starts (without film boiling) as confirmed previously [23].

### 3.2. Large Biot number comparison

The most rigorous surface convection quenching corresponds to flow dynamics results in negligible thermal resistance compared to the internal conduction resistance, i.e., high Biot number of Eq. (6). So, we expect the most effective cooling results to tend towards the 1-D transient conduction solution, Eq. (7). Using the IHCP heat flux, we calculate the heat transfer coefficient and the Biot number, and Fig. 13 shows the time-dependent Biot number for each quenching method. The forced immersion (green) and multiple-jet immersion (red) begin with  $Bi_L$  of about 5 and continuously increase with elapsed time. In particular,  $Bi_L$  of multiple-jet immersion reaches over 100 after 30 s. With a large Biot number, the surface temperature reaches the incoming coolant temperature, and we can use the analytical solutions of Eqs. (7) to (9) for the temperature, time rate of temperature change, and the surface heat flux. They have been used in all the figures representing the IHCP results for comparison.

Fig. 14(a) shows the surface heat flux history from Eq. (8) (large  $Bi_L$ ) and the IHCP approximation. The maximum value from Eq. (8) is 11 MW/m<sup>2</sup>, followed by a large decrease with increased elapsed time. The IHCP results for the multiple jet quenching give 5.2 MW/m<sup>2</sup> at 0.4 s, and at the same elapsed time, the large  $Bi_L$  results give 5.7 MW/m<sup>2</sup>. Initially, a high Biot number exists, as shown in Fig. 13, so the small heat flux by the IHCP method is due to the experimentally recorded response delay. There is good agreement between the results of the high Biot number method and the IHCP method for elapsed time larger than 0.5 s.

The large  $Bi_L$  limit shows the upper limit of the transient cooling rate of the plate and is given by the analytical forms, Eqs. (7) to (9). Fig. 14(b) compares the transient temperature distribution from Eq. (7) and with the IHCP method at several locations from the surface. The IHCP results include the experimental results as well as the interpolated values. A symbol and a dashed line indicate the predicted temperature by IHCP at a location. The large  $Bi_L$  prediction is based on a continuous variation of temperature. The large  $Bi_L$  surface (0 mm) temperature is the coolant temperature of 20 °C. However, the IHCP surface temperature uses the 1 mm and larger distances data to predict the surface temperature. Since the multiple-jet quench Biot number starts at 5, there may be some errors in this solution for early elapsed time (till Biot increases further), as shown in Fig. 13. So, larger elapsed time provides a more reasonable comparison, Fig. 14(b), and the difference vanishes as the elapsed time of 50 s is reached. The penetration time calculated by Eq. (10) is 46 s; however, the sample is cooled drastically by that time. We conclude that the IHCP method, which includes experiment data, underpredicts the surface heat flux compared to the large  $Bi_L$  prediction and has inherent uncertainties for elapsed time smaller than 0.5 s.

Fig. 12(b) compares the cooling rate from the large  $Bi_L$  prediction and the IHCP method. The large  $Bi_L$  results are the ideal cooling (the surface temperature is the same as the coolant temperature). This upper limit is shown in Figs. 6 to 14. In the IHCP

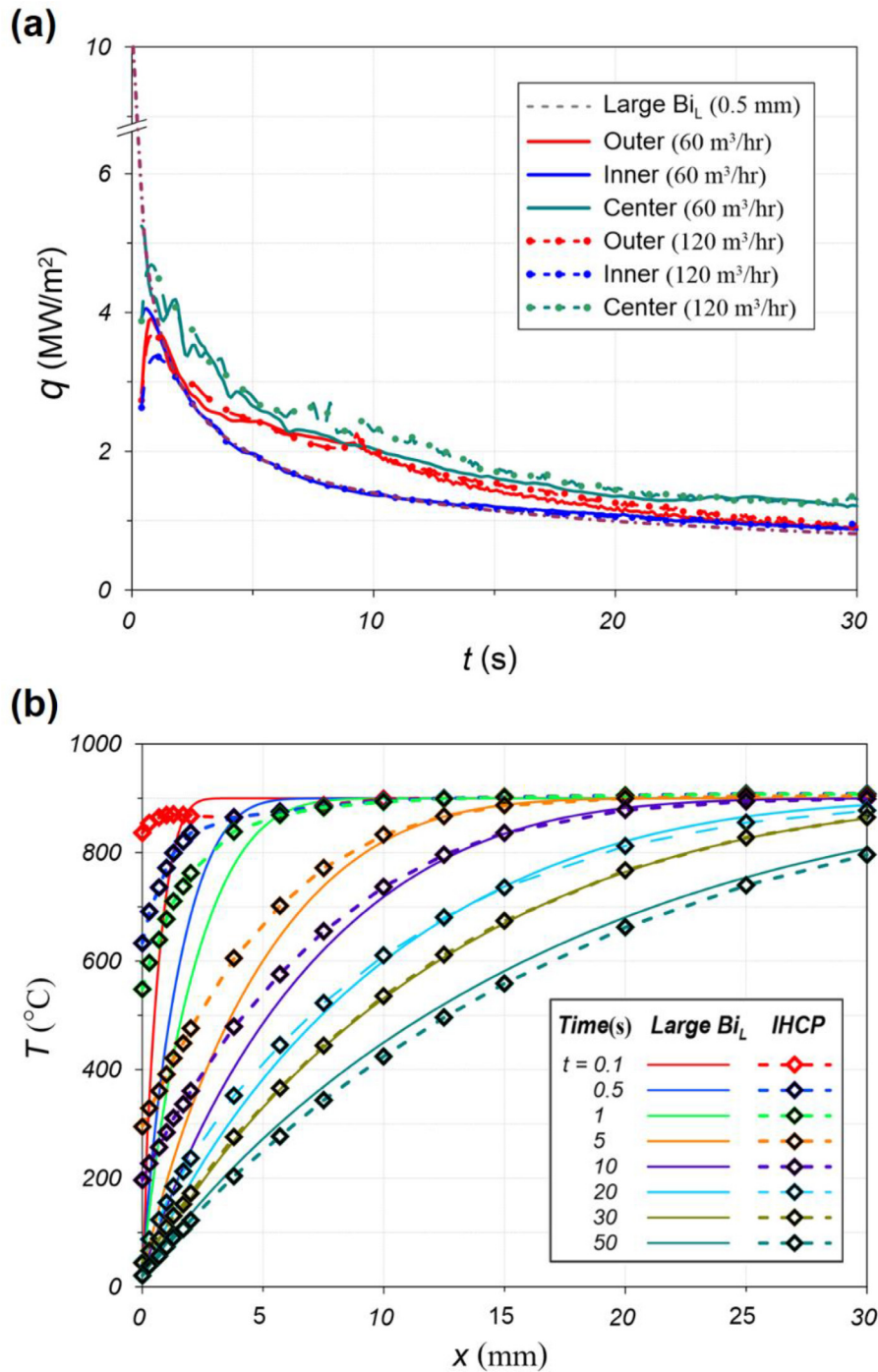


**Fig. 14.** Comparison of the (a) heat flux distribution and (b) temperature distribution for stainless steel (SUS310S) calculated by the large  $Bi_L$  and the IHCP methods for the multiple-jet quenching.

method, the sampling rate of the thermometer is 10 data/s, so the data measurement start is 0.1 s. The large  $Bi_L$  results at 0.5 and 1 mm depth give the upper limit of 10304 °C/s at 0.01 s and 2600 °C/s at 0.03 s, respectively. The IHCP results give a maximum value for the multiple-jet quench of 625 °C/s at 0.1 s, and this corresponds to 2 mm depth for the large  $Bi_L$  results (642 °C/s at 0.16 s).

### 3.3. Post quench surface microstructure and mechanical properties

The phase morphology of the quenched surface is observed with respect to the cooling performance, surface microstructure,

and mechanical properties. Fig. 15 shows the transient temperature distribution for the four quenching methods, 1 mm from the surface. Only nine holes are machined in the cube, Fig. 3(b)(ii), to allow for sufficient samples for microscopic tests. Three holes each on the top, lateral and bottom surfaces. As mentioned, the cooling performance of the bottom surface of water/oil immersion quenching shows a slow slope compared to the top and lateral surfaces, as shown in Fig. 15(a) and (b). In Fig. 15(c), the cooling rate of the top surface shows the most rapid cooling with the forced immersion quenching. The multiple-jet quenching result of Fig. 15(d) shows the most rapid cooling overall.

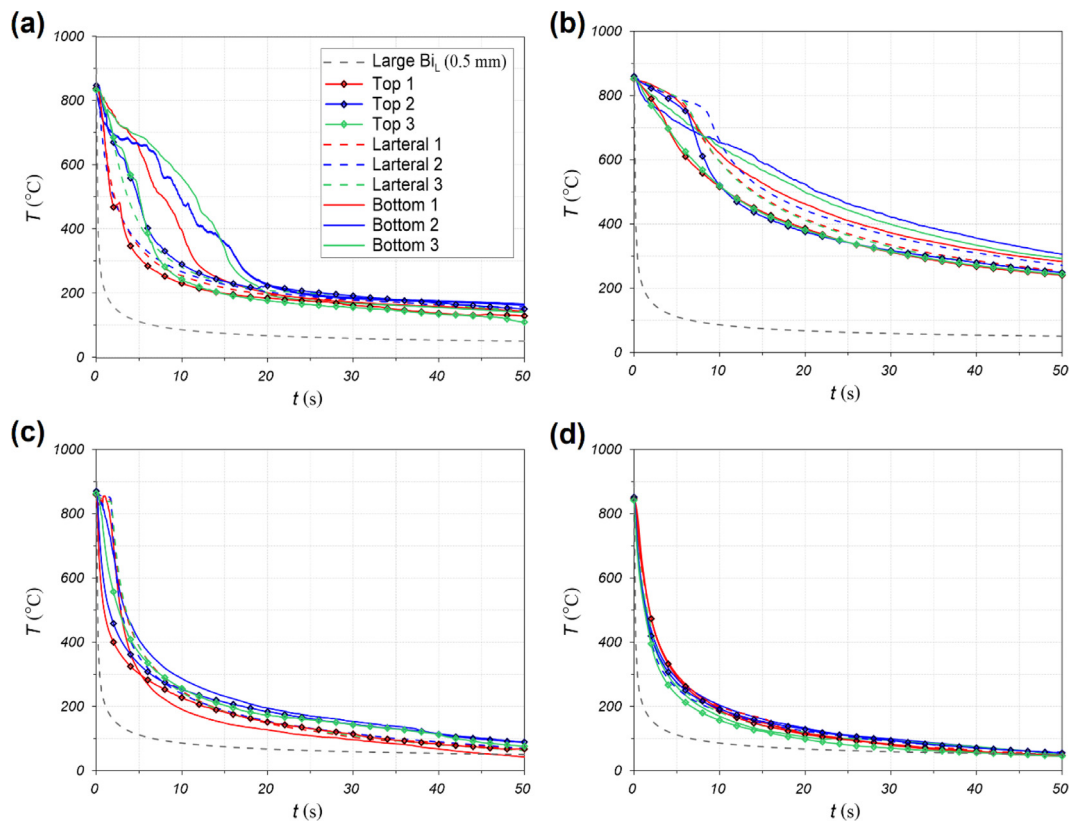


**Fig. 15.** Transient temperature distribution of SNCM439 alloy steel with four quenching methods (a) water immersion, (b) oil immersion, (c) forced immersion, and (d) multiple-jet quenching, at 1 mm from the surface.

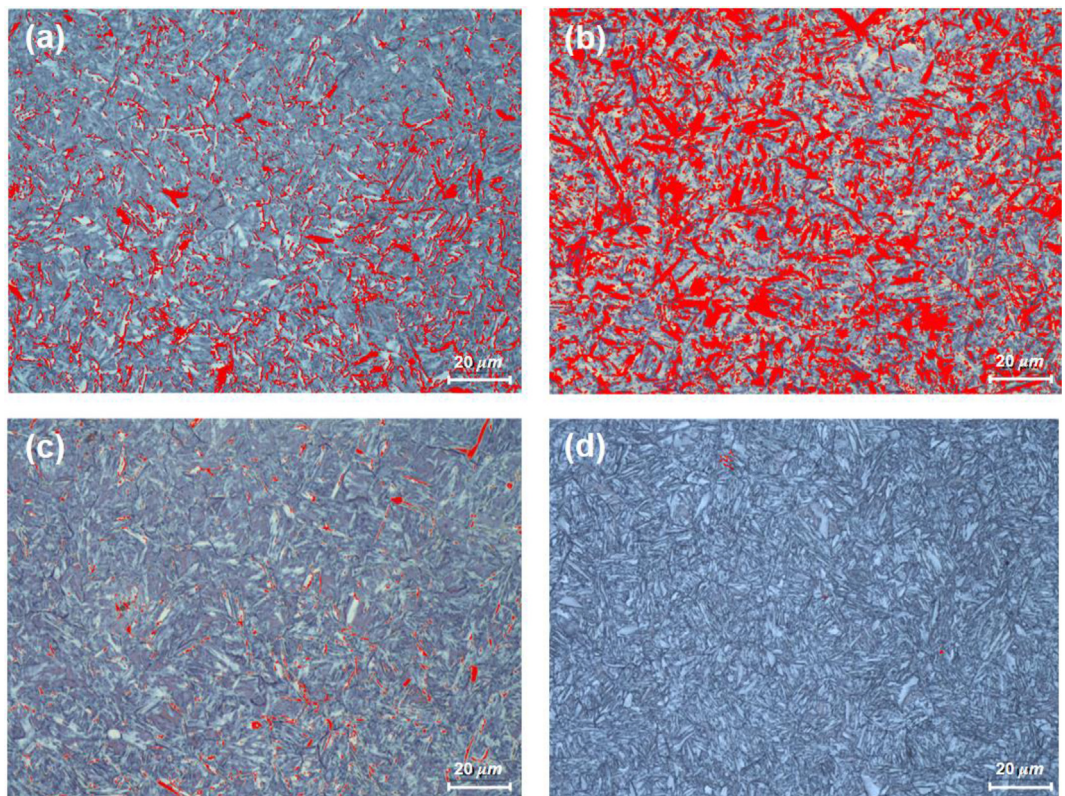


**Fig. 16.** SEM images of the quenched surface of SNCM439 alloy steel, where light blue and blue represent martensite and red for bainite phases, (a) water, (b) oil, (c) forced immersion, and (d) multiple-jet quenching.

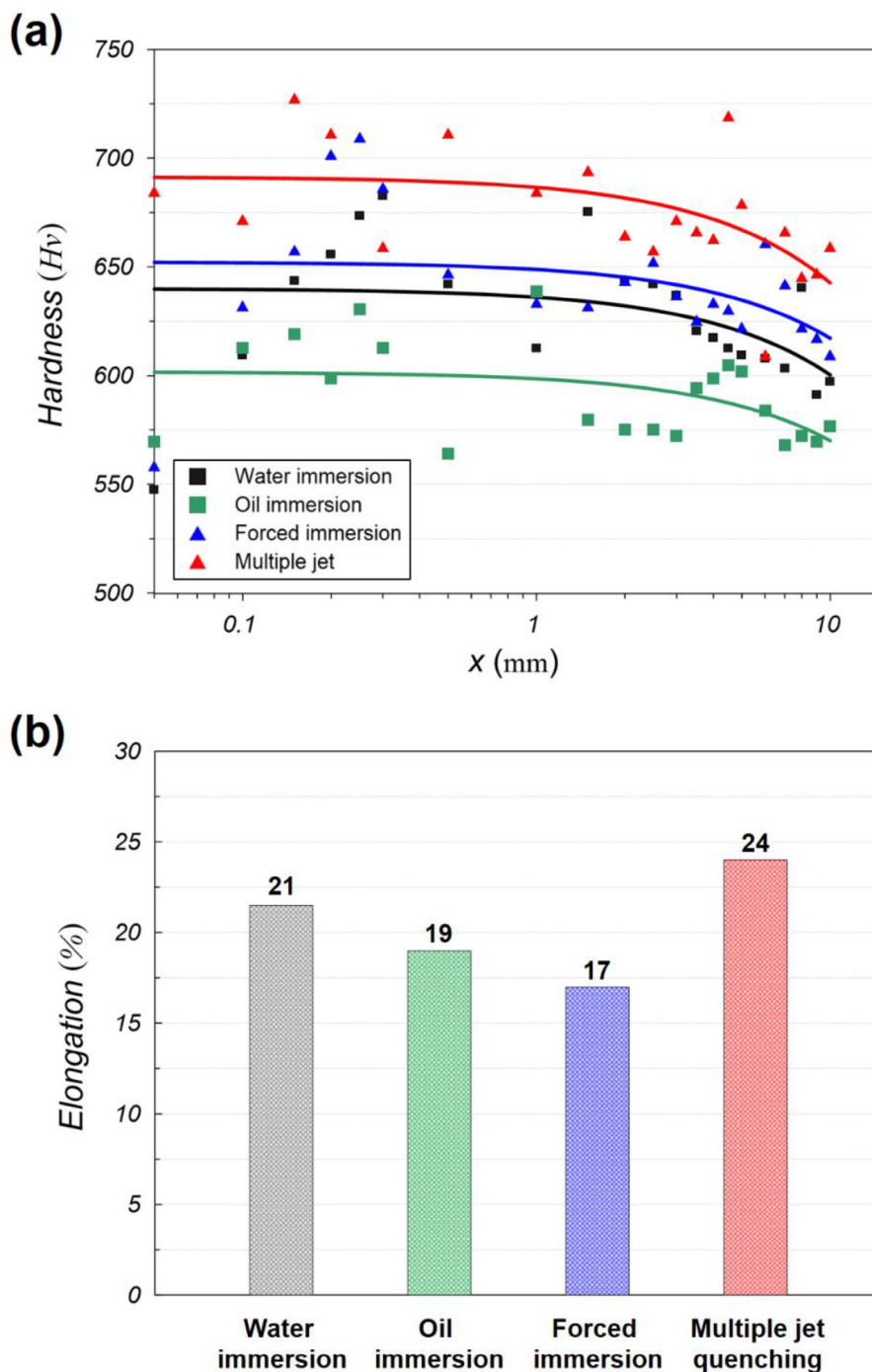


Fig. 17. (a) Hardness profile along with the depth and (b) surface elongation of after quenched SNCM439 alloy steel in various quenching methods.

The SEM micrographs of the post-quenched surface are shown in Fig. 16. The etched samples of the SNCM439 alloy steel were used for the microstructure observation. The SEM images were binarized to light blue and red to distinguish the martensite from the bainite phase. In this figure, light blue and blue parts represent the martensite and the red spot indicates the bainite phase. With the water and oil immersion quenching shown in Fig. 16(a) and (b), relatively large red spots of the bainite appear at a volume fraction of 8 and 27%. Whereas, with a high cooling rate of Fig. 16(c) and (d), the red spots are substantially reduced to 3% and 0.2% volume fractions. It is confirmed that the martensite phase is mainly formed with a high cooling rate. In particu-

lar, nearly 100% martensite phase is formed with the multiple jet quenching.

The mechanical properties, hardness, and sample elongation are presented in Fig. 17(a) and (b). Fig. 17(a) shows the hardness profile along with the distance from the surface with a trend line to view the profile. The largest value of 690 Hv is at the surface ( $x = 0$ ) for the multiple-jet quench, and the oil immersion shows the lowest value of 563 Hv. The forced immersion and water immersion results are similar, with the forced immersion resulting in a slightly better hardness. Constant hardness values are maintained with depth and then attenuate toward the 10 mm depth by only an average 6%. Fig. 17(b) shows the sample elongation af-

ter quenching. The multiple-jet quenching, which has the fastest cooling rate, shows the largest elongation of 24%, followed by the water and oil immersion and forced immersion. The forced immersion is expected to result in high elongation due to the relatively high cooling rate, but it has the lowest value. This method uses a large coolant flow rate, and the cooling time is the shortest compared to other methods until heat transfer to the interior proceeds.

#### 4. Conclusions

This study on boiling quenching uses four coolant hydrodynamic quenching methods, two steel types, along with 2-D and 1-D heat transfer analyses and post-quench material characterization, for the selection of the most effective quenching method. Comparison among the temperature distribution, local time rate of temperature change, and the surface heat flux show major differences among these quenching methods. For the water immersion, the high stirring of the coolant enhances the overall (overall surface) cooling rate. This enhancement in cooling rate does not appear with the highly stirred oil immersion, where a more uniform cooling is observed. The forced immersion increases the cooling rate while using a large coolant flow rate. It is found that the multiple-jet quenching induces the fastest cooling rate even at a relatively low flow rate. The high-momentum jet flow efficiently removes the vapor films, which cause thermal resistance. The methods are water multiple-jet, water forced, water and oil immersion in order of effectiveness.

A theoretical approximation is proposed based on the high Biot number behavior, which allows for the 1-D transient conduction analytical expression for the temperature distribution, local time rate of temperature change, and the surface heat flux. These can complement the numerical inverse heat conduction problem (IHCP) solution, which uses the measured temperature in pre-selected locations away from the surface. Good agreement is found between the two solutions under multiple-jet quenching and for elapsed times larger than 0.5 s.

The volume fraction of the martensite phase shows good agreement with the surface cooling rate of each quenching method. The SEM micrography results confirmed that the martensite phase is mainly formed with a high cooling rate, and a nearly 100% martensite phase is formed with the multiple-jet quenching. The investigation of the mechanical properties confirmed that the high cooling rate of the multiple-jet quenching induces the highest hardness and elongation. Figs. 1 and 15, which are for the SNCM39 steel, show that the rapid cooling is achieved by the multiple-jet quenching and results in the martensite phase, while the oil-immersion quenching results in moderate cooling and multiple microstructures.

#### Declaration of Competing Interest

We wish to confirm that there are no known conflicts of interest associated with this publication. There has been no significant financial support for this work that could have influenced its outcome.

#### CRediT authorship contribution statement

**Sang Gun Lee:** Conceptualization, Methodology, Validation, Formal analysis, Investigation, Visualization, Writing – original draft. **Massoud Kaviany:** Methodology, Formal analysis. **Jungho Lee:** Supervision, Funding acquisition, Resources, Writing – review & editing.

#### Acknowledgment

This work was supported by the National Research Foundation of Korea (NRF) grant funded by the Ministry of Science and ICT, Korea (No. NRF-2020R1A2C3008689).

#### References

- [1] V. Srinivasan, K. Moon, D. Greif, D.M. Wang, M. Kim, Numerical simulation of immersion quenching process of an engine cylinder head, *Appl. Math. Model.* 34 (2010) 2111–2128.
- [2] R. Kopun, L. Skerget, D. Zhang, B. Stauder, D. Greif, Numerical simulation of immersion quenching process for cast aluminum part at different pool temperatures, *Appl. Therm. Eng.* 65 (2014) 74–84.
- [3] J.J. Laskowski, W.E. Ranz, Spray quenching, *AIChE J.* 49 (1970) 802–816.
- [4] C. Li, S.V. Garimella, Prandtl-number effects and generalized correlations for confined and submerged jet impingement, *Int. J. Heat Mass Transf.* 44 (2001) 3471–3480.
- [5] D.H. Wolf, F.P. Incropera, R. Viskanta, Local jet impingement boiling heat transfer, *Int. J. Heat Mass Transf.* 39 (1996) 1395–1406.
- [6] D.E. Hall, F.P. Incropera, R. Viskanta, Jet impingement boiling from a circular free-surface jet during quenching: part 1. single-phase jet, *J. Heat Transf.* 123 (2001) 901–910.
- [7] W. Timm, K. Weinzierl, A. Leipertz, Heat transfer in subcooled jet impingement boiling at high wall temperatures, *Int. J. Heat Mass Transf.* 46 (2003) 1385–1393.
- [8] N. Karwa, L. Schmidt, P. Stephan, Hydrodynamics of quenching with impinging free-surface jet, *Int. J. Heat Mass Transf.* (2012) 3677–3685.
- [9] G. Spanos, R.W. Fonda, R.A. Vandermeer, A. Matuszeski, Microstructural changes in HSLA-100 steel thermally cycled to simulate the heat-affected zone during welding, *Metall. Mater. Trans. A* 26 (1995) 3277–3293.
- [10] S.I. Kim, Y. Lee, Influence of cooling rate and boron content on the microstructure and mechanical properties of hot-rolled high strength interstitial-free steels, *Met. Mater. Int.* 18 (2012) 735–744.
- [11] G.E. Totten, *Steel Heat Treatment: Metallurgy and Technologies*, CRC Press, 2006.
- [12] S.N. Abdullah, N. Sazali, A.S. Jamaludin, Study of low carbon steel in rapid cooling process: a short review, *J. Mod. Manuf. Syst. Technol.* 4 (2020) 52–59.
- [13] C.E. Bates, Selecting quenchant to maximize tensile properties and minimize distortion in aluminum parts, *J. Heat Transf.* 5 (1987) 27–40.
- [14] N.I. Kobasko, in: *Intensive Steel Quenching Methods. Theory and Technology of Quenching*, Springer-Verlag, New York, 1992, pp. 367–389.
- [15] M.A. Aronov, N.I. Kobasko, J.A. Powell, A.M. Freborg, B.L. Ferguson, Intensive quenching theory and application for imparting high residual surface compressive stresses in pressure vessel components, *J. Press. Vessel Technol.* 125 (2003) 188–194.
- [16] S. Vakili, M.S. Gadala, Boiling heat transfer of multiple impinging jets on a hot moving plate, *Heat Transf. Eng.* 34 (2013) 580–595.
- [17] S. Ishigai, S. Nakanishi, T. Ochi, Boiling heat transfer for plane water jet impinging on a hot surface, in: *Proceedings of the 6th International Heat Transfer Conference*, Toronto, Canada, 1978.
- [18] J. Hammad, Y. Mitsutake, M. Monde, Movement of maximum heat flux and wetting front during quenching of hot cylindrical block, *Int. J. Therm. Sci.* 43 (2004) 743–752.
- [19] S.G. Lee, M. Kaviany, C.J. Kim, J. Lee, Quasi-steady front in quench subcooled-jet impingement boiling: experiment and analysis, *Int. J. Heat Mass Transf.* 113 (2017) 622–634.
- [20] S.G. Lee, M. Kaviany, J. Lee, Quench subcooled-jet impingement boiling: two interacting-jet enhancement, *Int. J. Heat Mass Transf.* 126 (2018) 1302–1314.
- [21] T. Kim, D.W. Oh, K.H. Do, J.M. Park, J. Lee, Effect of initial temperature of a cylindrical steel block on heat transfer characteristics of staggered array jets during water jet quenching, *Heat Transf. Eng.* 36 (2015) 1037–1045.
- [22] S.G. Lee, J.S. Kim, D.H. Shin, J. Lee, Boiling heat transfer characteristics of staggered-array water impinging jets on hot steel plate, *J. Heat Transf.* 140 (3) (2018) 030903.
- [23] S.G. Lee, M. Kaviany, J. Lee, Quench subcooled-jet impingement boiling: staggered-array jets enhancement, *Int. J. Heat Mass Transf.* 136 (2019) 888–898.
- [24] B. Weigand, S. Spring, Multiple jet impingement a review, *Heat Transf. Res.* 42 (2) (2011) 101–142.
- [25] S. Twomey, The application of numerical filtering for the solution of integral equations encountered in indirect sensing measurements, *J. Frankl. Inst.* 279 (1965) 95–109.
- [26] J.V. Beck, B. Blackwell, C.R. St. Clair, *Inverse Heat Conduction*, Wiley, New York, 1985.
- [27] C.F. Gomez, C.W.M. van der Geld, J.G.M. Kuerten, M. Bsbisi, B.P.M. van Esch, Film boiling in quench cooling with high-temperature jets, *Int. J. Heat Mass Transf.* 164 (2021) 120578.
- [28] F.M. Tenzer, I.V. Roisman, C. Tropea, Fast transient spray cooling of a hot thick target, *J. Fluid Mech.* 881 (2019) 84–103.
- [29] ISOGuide to the Expression of Uncertainty in Measurement, International Organization for Standardization, Geneva, 1995.

- [30] B. Blackwell, J.V. Beak, A technique for uncertainty analysis for inverse heat conduction problems, *Int. J. Heat Mass Transf.* 53 (2010) 753–759.
- [31] M. Kaviany, *Essentials of Heat Transfer*, Cambridge University Press, New York, 2011.
- [32] M. Takahashi, H. Bhadeshia, H.L.D.H. Bhadeshia, Model for transition from upper to lower bainite, *Mater. Sci. Technol.* 6 (1990) 592–603.
- [33] F.S. LePera, Improved etching technique for the determination of percent martensite in high-strength dual-phase steels, *Metallography* 12 (1979) 263–268.
- [34] T. Giordani, T.R. Clarke, C.E.F. Kwietniewski, M.A. Aronov, N.I. Kobasko, G.E. Totten, Mechanical and metallurgical evaluation of carburized, conventionally and intensively quenched steels, *J. Mater. Eng. Perform.* 22 (2013) 2304–2313.